mater.scichina.com link.springer.com

Published online 5 March 2024 | https://doi.org/10.1007/s40843-023-2787-5
Sci China Mater 2024, 67(4): 1332–1339

Fabrication of flexible silica aerogel composite blankets from an aqueous fumed silica-based slurry

Shunyao Zhang, Lukai Wang, Junzong Feng*, Yonggang Jiang, Liangjun Li, Yijie Hu and Jian Feng

ABSTRACT Silica aerogels exhibit considerable potential for thermal insulation applications owing to their low thermal conductivity. However, they generally possess poor mechanical properties and need to be mechanically enhanced while maintaining their low thermal conductivity. In this study, commercial fumed silica and methyltrimethoxysilane were used as the silica sources and water and ethanol were used as solvents to form a slurry. Consequently, silica aerogel monoliths (SAMs) were prepared through ambient drying without additional surface modification or solvent replacement. The resulting SAM maintained a typical nanopore structure and exhibited low density (0.24 g cm^{-3}), shrinkage (4%), and thermal conductivity (0.046 W m^{-1} K^{-1}). The slurry was impregnated with fiber blankets *via* roller pressing, and silica aerogel blankets (SABs) were prepared through thermal solidification of the slurry and ambient drying. The prepared SABs exhibited good flexibility and mechanical properties, facilitating their installation and application for thermal insulation and considerably reducing production cycles and costs. In addition, controlling the particle size and mass fraction of opacifiers decreased the high-temperature thermal conductivities of SABs owing to the nanopore structure and low shrinkage of SAMs, and the thermal conductivity of the optimized SAB at 800°C was as low as 0.054 W m^{-1} K^{-1}.

Keywords: silica aerogel, flexible blanket, ambient drying, thermal insulation

INTRODUCTION

Silica aerogels have demonstrated exceptional performance in various applications owing to their network structure at the nanoscale, high specific surface area (500–1200 m^2 g^{-1}) [1], and high porosity (85%–99.8%) [2] as well as low density (0.03–0.35 g cm^{-3}), thermal conductivity (0.01–0.03 W m^{-1} K^{-1}) [3], refractive index (1.00–1.08) [4], and dielectric constant (1.0–2.0) [5]. These unique properties have led to their use in various applications, such as thermal and acoustic insulation [6–10] and gas adsorption [11], and purposes, such as ensuring building energy efficiency [12,13] and the aerospace industry [14–17]. However, they cannot be directly applied as thermal insulation materials because of their brittleness and poor mechanical properties. Currently, fibers with high mechanical strength are being used to reinforce silica aerogels to form composites and to improve their mechanical properties [18–20].

Two methods have been mainly used for preparing silica aerogel–fiber composites. The first method is to directly press the silica aerogel powder, short fibers, and binder together using mechanical pressure [21,22], thereby obtaining their fiber-reinforced composites. The second method is to impregnate fiber blankets or preforms with a silica sol and performs a series of gelation, aging, and drying processes to obtain the composite materials [23,24]. Although the first method is relatively simple, the low strength of the composites prepared using simple mechanical forces as well as their installation performance and vibration resistance are poor owing to the short fiber size. The second method offers reinforcement *via* fiber blankets or preforms, which can improve the mechanical properties of the prepared composites, as well as their installation and applicability. However, this method usually requires the use of supercritical drying technology performed in a high-temperature and high-pressure environment using specialized equipment, resulting in a more complex preparation process and high production costs. Thus, there is still a need to develop a new process to prepare low-cost silica aerogel composites without compromising their low thermal conductivity and maintaining their satisfactory mechanical properties.

The slurry molding method involves the preparation of a silica slurry by mixing prefabricated nanosilica powder (e.g., fumed silica powder and silica aerogel powder) and a solvent and impregnating the slurry into a fiber blanket. Subsequently, the solvent is removed from the blanket to form a silica aerogel composite. This method directly uses nanosilica powder as the silica source, which is more economical than the traditional sol-gel method involving ambient drying [25–27]. For example, Lee *et al.* [28] formed a stabilized slurry of silica aerogel powder in a mixed ethanol-water solution containing a polyvinyl alcohol binder and then prepared low-density silica aerogel composite blankets with thermal conductivities as low as 0.019 W m^{-1} K^{-1} *via* impregnation. However, due to the use of a polyethylene blanket, the composites were not temperature-resistant.

Among these nanosilica powders, in recent years, fumed silica has been used for preparing silica aerogels and their composites owing to its unique three-dimensional (3D) network structure, nanopore size distribution, and low cost [29]. For instance, Xia *et al.* [30] proposed a new method combining interfacial modification and ultralow-concentration sol impregnation to adjust the pore structure of fumed silica compacts and reduce their thermal conductivity. Their results showed that the pore size and volume fraction of the macropores of the treated fumed

Science and Technology on Advanced Ceramic Fibers and Composites Laboratory, College of Aerospace Science and Engineering, National University of Defense Technology, Changsha 410073, China
* Corresponding author (email: junzongfeng@nudt.edu.cn)

silica compacts were considerably reduced and the thermal conductivity decreased from 0.027 to 0.022 W m^{-1} K^{-1}. Our group [31] demonstrated a thermal solidification-based 3D-printing strategy to produce a silica aerogel with a complex structure by directly writing a silica ink. The ink used for printing comprised fumed silica powder and hydrosol. The optimized 3D-printed specimen exhibited a high specific surface area of 272 m^2 g^{-1} and low thermal conductivity of 0.032 W m^{-1} K^{-1}. Pure fumed silica had a high infrared radiation transmittance at high temperatures; therefore, the thermal conductivity of fumed silica increased dramatically as the temperature increased. Doped opacifiers (such as SiC, ZrO_2, and TiO_2) can effectively inhibit radiative heat transfer and improve the high-temperature thermal insulation performance of fumed silica-based insulation materials [32,33]. Du *et al.* [34] prepared a zirconia fiber-glass fiber and fumed silica-based thermal insulation material using a dry pressing method. The zirconia fibers enhanced the mechanical properties and suppressed the radiative heat transfer of the composites, thereby reducing the high-temperature thermal conductivity of the composites.

Herein, we present a low-cost and rapid ambient drying method for preparing silica aerogel composite blankets (SABs). Commercial fumed silica and methyltrimethoxysilane (MTMS) were used as the silica sources, and glass fiber-needled blankets were used for reinforcement. The formulation of fumed silica and MTMS into a slurry and then compounding it with fiber blankets helped the ambient drying preparation and cost reduction of SABs. Fumed silica acted as a template orientation agent for the induced growth of nanoparticle networks originating from MTMS, imparting ambient-dried silica aerogel monoliths (SAMs) with a remarkable nanopore feature [35]. Owing to the hydrophobicity of fumed silica and the methyl group in MTMS, the ambient-dried SAMs exhibited low density and shrinkage, resulting in SABs with low thermal conductivity. In addition, to reduce the high-temperature thermal conductivity, we doped SiC opacifiers with different particle sizes and mass fractions and investigated the effects of the opacifiers on the high-temperature thermal insulation properties of the composites. The optimized SAB showed low thermal conductivity at both low and high temperatures as well as excellent flexibility and mechanical properties, which can facilitate its use and installation in a variety of scenarios, making it an ideal thermal insulation material for diverse applications.

EXPERIMENTAL SECTION

Materials

Hexamethyldisilazane (HMDS) was purchased from Shanghai Aladdin Biochemical Technology Co., Ltd. (China). Fumed silica (hydrophilic, with a specific surface area of ~200 m^2 g^{-1}), MTMS (98%), urea (99%), and anhydrous ethanol were purchased from Shanghai Macklin Biochemical Technology Co., Ltd. (China). A glass fiber-needled blanket with a thickness of 3 mm was purchased from Langfang Ke'an Sealing Materials Co., Ltd. (China). Deionized water with a resistivity of 18.2 MΩ cm was used.

Hydrophobic modification of fumed silica

The hydrophilic fumed silica powder and excess HMDS (more than 20 wt% of fumed silica) were placed in a closed container and heated in an oven for hydrophobic modification at 80°C for 12 h, where HMDS reacted with the surface hydroxyl groups of fumed silica, increasing the hydrophobicity of fumed silica upon the formation of a large number of methyl groups on its surface. This process was followed by heat treatment at 80°C for 12 h to remove the residual HMDS from the surface of fumed silica and obtain the hydrophobic fumed silica powder.

Preparation of SAMs and SABs

First, MTMS was hydrolyzed in an acid environment, an aqueous solution of 30 wt% EtOH was added to MTMS under magnetic stirring conditions, and 0.1 mol L^{-1} nitric acid was slowly added dropwise to adjust the solution pH to 3. After continuous stirring for 30 min, 0.2 wt% urea was added to the MTMS solution to obtain the MTMS sol. Subsequently, a certain amount of hydrophobic fumed silica and opacifiers were added, and the silica slurry was obtained upon planetary mixing, during which air bubbles in the slurry were removed *via* centrifugation. The solid content of the hydrophobic fumed silica in the slurry was kept constant at 10 wt%, and the solid content of MTMS was kept constant at 20.3 wt% to ensure that the solid content of the silica aerogel generated using MTMS was equal to that of fumed silica. Finally, SAMs and SABs were prepared as follows: (1) silica slurry was heated in a water bath at 60°C, solidified and aged through the polycondensation reaction for 24 h, placed in an oven at 60°C, and dried at ambient pressure for 2 days to obtain SAMs. (2) Silica slurry was impregnated with glass fiber-needled blankets using roller pressing. First, the slurry was poured into the mold with a roller. The fiber blanket moved forward continuously with the rotation of the roller and was completely immersed in the slurry. Then, the slurry was fully immersed in the fiber blanket under the shear force of the roller. Similarly, impregnated fiber blankets were heated in a water bath at 60°C for 24 h, placed in an oven at 60°C, and dried at ambient pressure for 2 days to obtain SABs.

Two series of samples were prepared by changing the particle size and the solid content of the opacifier: 1-wt% SiC content was used in the slurry using SiC particle sizes of 1, 2, 3, and 5 μm. In addition, a fixed SiC particle size (3 μm) was selected, and the SiC content in the slurry was varied to 1%, 2%, and 3%. The number of SAM samples was denoted as SAM-*x*%-*y* μm, and the number of SAB samples was denoted as SAB-*x*%-*y* μm, where *x* is the percentage of the SiC content in the slurry and *y* is the SiC particle size.

Characterization

The vernier caliper was used to measure the diameter of the solidified slurries, SAMs, and SABs. The samples were weighed and calculated to obtain their linear shrinkage and apparent density values. The room-temperature thermal conductivities of SAMs were determined using a thermal constant analyzer (Hot disk, TPS 2500S) with the test probe c5465. The chemical analysis of the surface elements of the samples was performed using an X-ray photoelectron spectrometer (XPS, Thermo Fischer, ESCALAB 250Xi). The rheology of the slurries at 25°C was measured using a rotational rheometer (MCR302, Anton Paar) with a 25-mm-diameter steel plate and a gap height of 0.5 mm. A field-emission scanning electron microscope (SEM, ZEISS, Sigma 300) was used to observe the microscopic morphology of the samples. Nitrogen adsorption-desorption isotherms were calculated at 77 K using a Quantachrome ASiQwin surface area and porosimetry analyzer (Quantachrome, Autosorb-iQ2-MP). An automatic mercury porosimeter (Quantachrome, PoreMaster

33) was used to test the specific surface areas and pore size distributions of the samples. The Fourier transform infrared (FTIR) spectra of the samples were measured in the wavenumber range of 400–4000 cm^{-1} using an infrared spectrometer (Thermo Fisher, Nicolet 6700). The thermal gravimetric (TG) differential scanning calorimetry (DSC) curves of the samples were obtained using a simultaneous thermal analyzer (PerkinElmer, STA 8000). The water contact angle was measured using a contact angle instrument (KRUSS, DSA100). The room-temperature thermal conductivities of SABs were tested using a thermal conductivity measuring instrument (Fox 200). The high-temperature thermal conductivities of SABs were tested using the water flow plate method (PBD-13-4P, China) at 200, 400, 600, and 800°C. The compressive and tensile strengths of the samples were tested using a mechanical tester (FULE TEST). The hot and cold side temperatures of 10-mm-thick samples at high temperatures (600 and 800°C) were recorded using a quartz lamp radiation heater.

RESULTS AND DISCUSSION

Preparation of SAMs and SABs

The preparation of SAMs and SABs is shown in Fig. 1. During the preparation process, fumed silica was used as a template for growing a nanoporous silica network, which can induce MTMS to generate a nanoparticle stacking network on the fumed silica skeleton [35]. Because of the strong hydrophobicity of fumed silica, a certain amount of ethanol was added to the solvent to ensure uniform mixing of the raw materials in the slurry. The slurry exhibited shear thinning, a non-Newtonian fluid behavior (Fig. S1), and its viscosity decreased with increasing shear rate. In addition, the energy storage modulus of the slurry was higher than the loss modulus ($G' > G''$). These two properties ensured that the slurry could be immersed into the fiber blankets after shearing using the rollers, and the viscosity increased after the shear force disappeared, which ensured that the slurry did not flow out of the fiber blankets. The solidification of the slurry was controlled *via* the thermal decomposition of urea at 60°C, endowing the slurry with controllable properties and ensuring that the slurry did not solidify before rolling and impregnating the fiber blanket.

Fig. 2a shows the optical photographs of SAMs incorporating opacifiers with different particle sizes. Despite the presence of a few cracks on the surface of SAMs, they still have good formability, and these cracks would have a minimal effect on the performance of SABs. The XPS results showed that after hydrophobic modification, the oxygen content on the surface of fumed silica decreased, whereas the carbon content increased (Table S1). The photoelectron peaks of hydrophilic and hydrophobic fumed silica further indicated that the hydroxyl group of fumed silica decreased, whereas the methyl group increased (Fig. S2). Owing to the hydrophobic modification of fumed silica and the hydrophobic effect of the methyl groups of MTMS, the densities of the ambient-dried SAMs were as low as 0.24 g cm^{-3} and their linear shrinkage values were as low as 4% (Fig. 2b). The thermal conductivities of the SAMs involving opacifiers with different particle sizes at room temperature are shown in Fig. 2c. The results showed that the thermal conductivities of the SAMs obtained using opacifiers with particle sizes of 2 and 3 μm were lower, reaching the lowest value of 0.046 W m^{-1} K^{-1}.

Pore structure features

The SEM images of SAMs are shown in Fig. S3. The SiC particles are tightly wrapped inside the silica aerogel, and almost no crack is observed at the interface between SiC and the aerogel, indicating that the silica aerogel can react and grow along the surface of the opacifier. The results of the nitrogen adsorption-desorption tests showed that the silica aerogels were dominated by a mesoporous distribution with a few micropores and macropores (Fig. S4). The particle size of the opacifiers exhibited almost no effect on the specific surface area of the silica aerogel (Table S2); however, the average pore size and pore volume increased slightly with increasing SiC particle size. This may be because a small SiC particle size fills part of the macropores, decreasing the pore size and volume, whereas a large SiC particle size can only be encapsulated inside the aerogel, increasing the pore size and

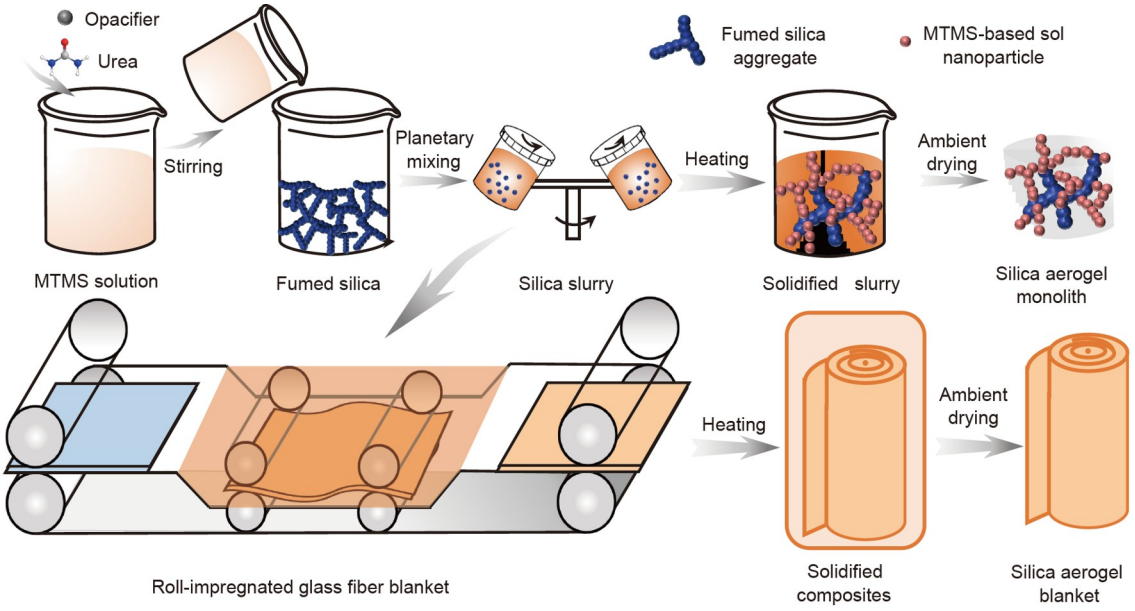

Figure 1 Schematic depicting the preparation process of SAMs and SABs using the slurry molding method.

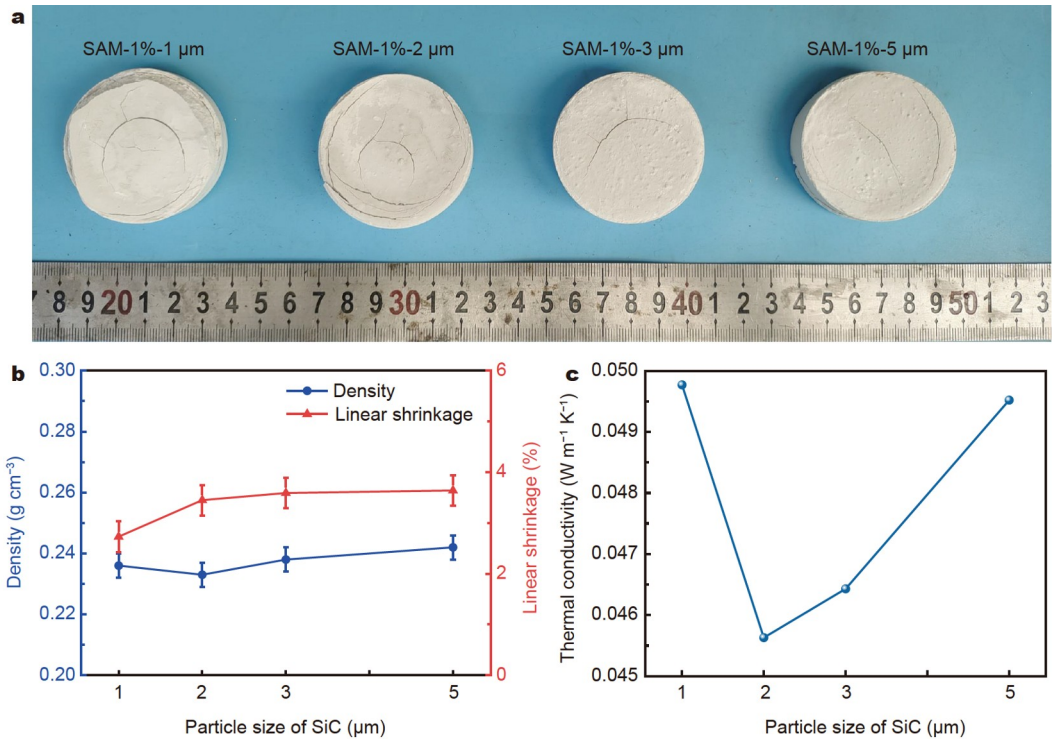

Figure 2 (a) Photographs, (b) density and linear shrinkage, and (c) room-temperature thermal conductivity values of SAMs obtained using SiC particles with different sizes.

volume.

The SEM images of SABs are shown in Fig. 3. The silica aerogel is tightly bound around the glass fibers, almost filling the space between them. The SEM image obtained at high magnification shows that the interior of the silica aerogel presents a 3D network formed by the assembly of nanoparticles and nanopores, with a "pearl chain" skeleton structure. Notably, under the induction of fumed silica, the silica aerogel particles present a uniform nanospherical structure and the particle size is controlled below 50 nm. The mercury porosimetry analyses of SAM and SAB show that SAM is primarily mesoporous, the pore size of SAM is concentrated at ~33 nm, and the pore size distribution of the glass fiber blanket is in the range of 2–10 μm (Fig. 4a). Compared with SAM and the glass fiber blanket, SAB contains more macropores. Although the pore size increases in SAB, the pore size of SAM is considerably lower than the average free path of gas molecules, which is beneficial for suppressing gas heat transfer.

Chemical composition

The energy-dispersive spectroscopy results show that the ambient-dried silica aerogel primarily comprises three elements, Si, O, and C, with a relatively uniform distribution (Fig. 3e–h), indicating that the raw materials were well mixed in the slurry system and the fumed silica powder did not settle owing to gravity during the slurry solidification process. Fig. 4b shows the FTIR spectra of MTMS, SAB, and fumed silica. The silane (Si–O–C) characteristic peaks located at 1191 and 1087 cm^{-1} disappeared [36], and broader characteristic absorption peaks of silicon oxide (Si–O–Si) were observed at 1105, 1032, and 781 cm^{-1} [37], indicating that MTMS underwent sufficient hydrolysis–condensation reactions catalyzed by nitric acid and urea. According to the XPS results, the oxygen content of SAM is lower than that of the hydrophobically modified fumed silica, indicating that the hydroxyl groups on the fumed silica skeleton participate in the polycondensation reaction during the solidification process. In addition, the Si–CH_3 absorption peak is observed at 1268 cm^{-1} for MTMS [38–40], fumed silica, and SAB. Moreover, the presence of the methyl group helps to reduce the solid–liquid interfacial force as well as avoid the severe shrinkage of the aerogel skeleton caused by the high capillary stress during the ambient drying process, thereby reducing the density and shrinkage of the ambient-dried silica aerogel. The water contact angle indicates that the prepared SAB exhibits good hydrophobicity with a contact angle of 136° (Fig. 4c).

To further characterize the chemical composition of the sample, SABs was analyzed for thermal stability, and the TG-DSC curves measured under an air atmosphere are shown in Fig. 4d. The weight loss process of SABs can be divided into three stages. The first stage occurs in the range of 0–100°C, where there is an upward heat absorption peak in the DSC curve. The weight loss rate is ~1%, which is primarily due to the heat absorption evaporation of the residual water inside SABs. The second stage is located in the range of 250–550°C, and the weight loss rate is ~2%–3%, which is mainly caused by the endothermic decomposition of residual urea and the oxidation of hydrocarbons. The third stage is located in the range of 550–800°C, the weight loss rate is ~2%, and there is a downward exothermic peak in the DSC curve, which is primarily due to the fracture of the Si–C bond and the removal of residual carbon [31,41]. The total weight loss rate of SAB at 1000°C is only 5%–6%, indicating that SAB possesses satisfactory thermal stability. In addition, the line shrinkage of SAB is only 1.4% after 4 h of heat treatment at 800°C, and SAB does not show sharp diffraction peaks before and after the heat treatment at 800°C

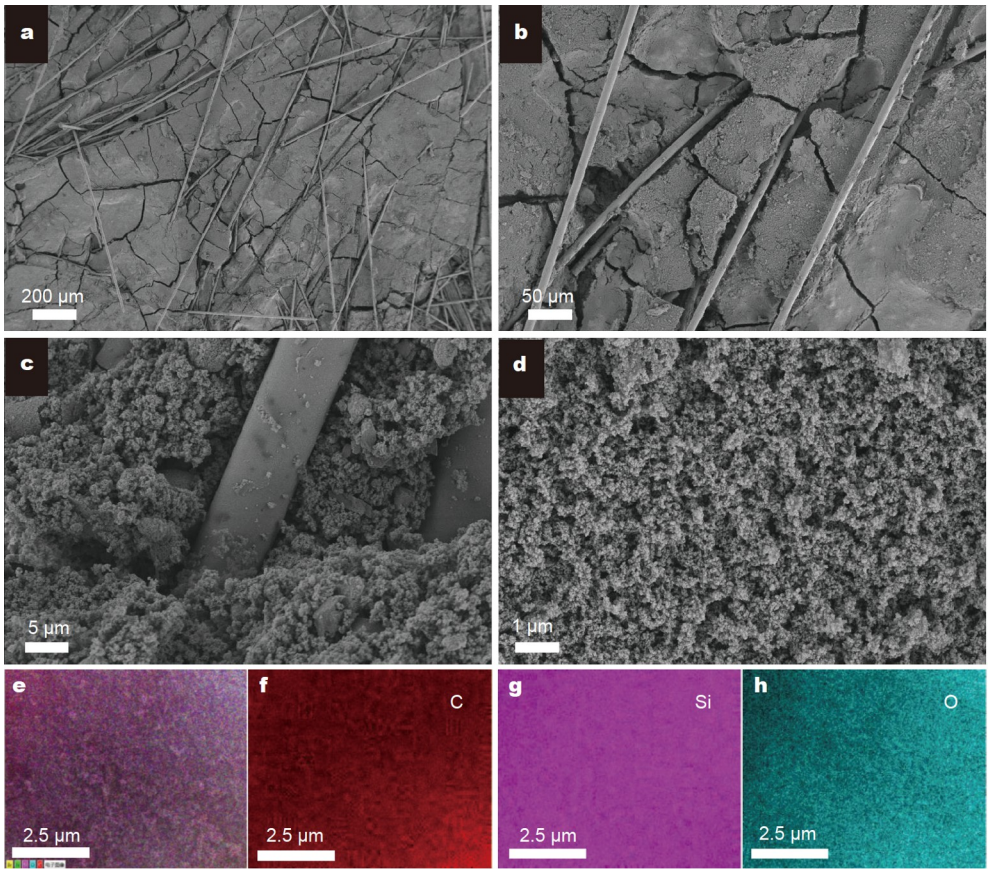

Figure 3 Microscale and nanoscale SAB morphologies. (a–d) SEM images of SABs. (e–h) Element distribution of the silica aerogel.

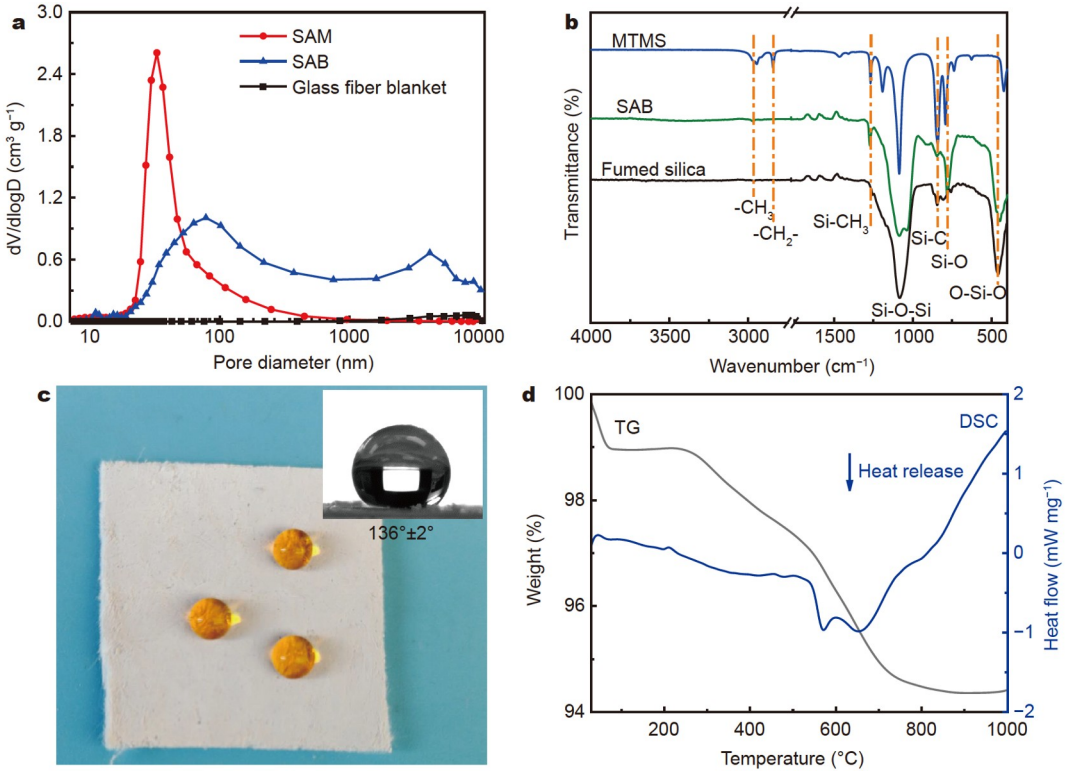

Figure 4 (a) Pore size distributions of SAM, SAB, and glass fiber blanket. (b) FTIR spectra of MTMS, SAB, and fumed silica. (c) Water contact angle of SAB. (d) TG-DSC curve of SAB.

(Fig. S5), with one diffraction peak near 2θ = 22° that corresponds to amorphous silica, indicating that the composites do not generate other crystalline structures and that SAB can be used at temperatures of up to 800°C for extended periods.

Mechanical properties

The compressive and tensile strengths of the glass fiber blanket and SAB are shown in Fig. 5. The compressive and tensile strengths of SAB are considerably improved compared with those of the glass fiber blanket. The compressive strength of SAB is 0.088 MPa under 10% deformation, and its compressive strength is 0.78 MPa under 60% deformation and is unchanged after 10 compression cycles, indicating that SAB has flexibility and good compression resilience. In addition, the maximum tensile strength of SAB is 0.65 MPa, which is much higher than that of the glass fiber blanket, indicating that the silica aerogel–fiber blanket composite improves the strength of SAB while maintaining good flexibility. Owing to these properties, SAB can be easily installed and used in a variety of thermal insulation scenarios (Fig. S6).

Thermal insulation properties

Owing to the low density and shrinkage of the SAMs prepared from the silica slurry, the thermal conductivity of SABs was considerably reduced. In addition, the prepared silica aerogel exhibited a mesoporous pore size distribution, which could effectively inhibit gas heat transfer and reduce the gaseous thermal conductivity of SABs. However, the silica aerogel suffered from high infrared radiation transmittance at high temperatures, requiring the addition of opacifiers to inhibit radiative heat transfer during the preparation process. The density and room-temperature thermal conductivity values of SABs prepared using different slurries are shown in Table S3. The change in SiC particle size had a negligible effect on the density and room-temperature thermal conductivity of SAB; however, as the SiC content increased, the density and room-temperature thermal conductivity of SAB gradually increased. The high-temperature thermal conductivities of SABs involving opacifiers with different particle sizes and without opacifiers are shown in Fig. 6a. The high-temperature thermal conductivities of SABs decreased considerably after the addition of SiC opacifiers and gradually decreased with increasing SiC particle size at 600 and 800°C. This phenomenon can be explained by the fact that the corresponding infrared wavelength range is 2.71–6.15 μm for the temperature range of 200–800°C [42]. According to the Mie scattering theory, an excellent scattering effect can be obtained for objects with similar sizes and wavelengths.

To prevent the increase in thermal conductivity induced by the large particle size of the SiC opacifiers, a particle size of 3 μm was selected, and the high-temperature thermal conductivity of SABs with different SiC contents is shown in Fig. 6b. The results show that an appropriate increase in the opacifier content is beneficial in reducing the radiant thermal conductivity as well as the high-temperature thermal conductivity of SABs. When excessive opacifiers were added, the thermal conductivity of SAB increased because of the increased solid thermal conductivity. The optimized SAB exhibited a thermal conductivity of 0.041 W m^{-1} K^{-1} at 600°C and 0.054 W m^{-1} K^{-1} at 800°C. Compared with the rigid silica aerogel composite product (KDMSG-1) with similar density prepared by supercritical drying in our group, it has the advantages of low cost and flexibility despite a slightly higher thermal conductivity. The thermal insulation properties of the optimized SAB were further characterized for 30 min using a quartz lamp at 600 and 800°C, and the results are shown in Fig. 6c, d, respectively. The cold side temperature of a 10-mm thick sample under thermal examination at 600°C rises to 139°C in 10 min and then slowly increases to 198°C, which is much better than that of the glass fiber blanket. The cold side temperature under thermal examination at 800°C increases to 190°C in 10 min, followed by a slow increase to 265°C, further indicating good thermal insulation properties of the prepared SAB.

CONCLUSIONS

Herein, we demonstrated a low-cost, rapid, ambient drying method for preparing SABs, wherein commercial fumed silica is hydrophobically modified and mixed with MTMS to form a slurry. The prepared SAMs exhibited a typical nanopore structure as well as low density (0.24 g cm^{-3}), shrinkage (4%), and thermal conductivity (0.046 W m^{-1} K^{-1}) at room temperature. Upon compounding the slurry with glass fiber blankets, the prepared SABs possessed both flexibility and promising mechanical properties, with a compressive strength of 0.78 MPa under 60% deformation and satisfactory compressive resilience, and the maximum tensile strength was 0.65 MPa. In addition, the optimized SAB exhibited excellent thermal insulation properties and thermal stability, with a total weight loss of only 5%–6% at 1000°C and a shrinkage of 1.4% at 800°C. The particle size and content of SiC remarkably affected the high-temperature thermal conductivities of SABs. When 2 wt% of 3 μm SiC

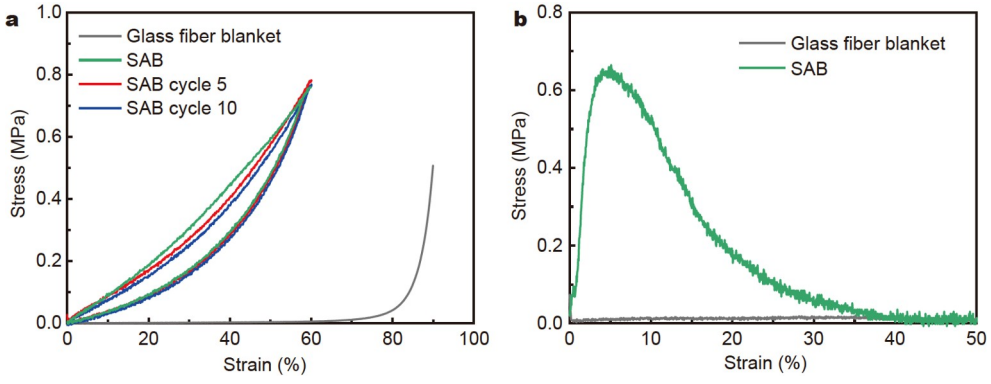

Figure 5 (a) Compressive and (b) tensile stress-strain curves of the glass fiber blanket and SAB.

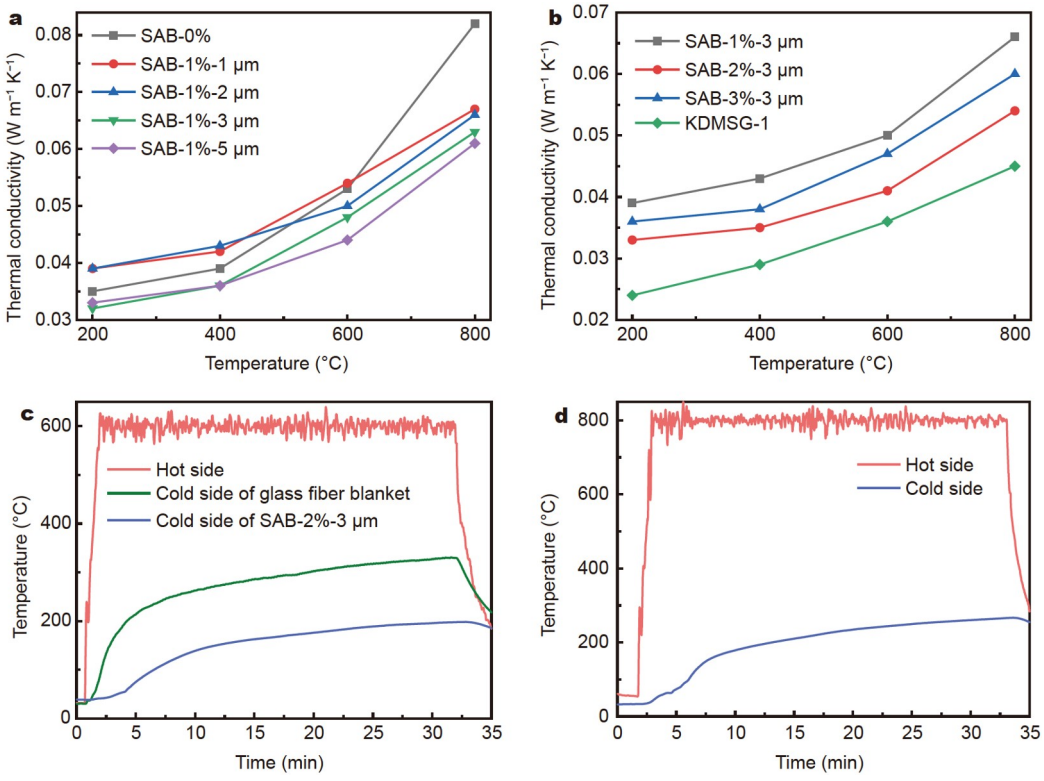

Figure 6 (a, b) High-temperature thermal conductivities of SABs with different (a) particle sizes and (b) contents of SiC opacifier. (c, d) Hot and cold side temperatures of the optimized SAB under a quartz lamp at (c) 600 and (d) 800°C.

was added, SABs demonstrated a thermal conductivity of 0.041 W m^{-1} K^{-1} at 600°C and 0.054 W m^{-1} K^{-1} at 800°C, making it an ideal thermal insulation material. More importantly, the slurry molding method proposed in this study can be extended to other silica nanopowders, paving the way for preparing ceramic powder-derived silica aerogel composites as thermal insulation materials.

Received 15 November 2023; accepted 24 January 2024; published online 5 March 2024

1 Soleimani Dorcheh A, Abbasi MH. Silica aerogel; synthesis, properties and characterization. J Mater Processing Tech, 2008, 199: 10–26
2 Li C, Chen Z, Dong W, *et al.* A review of silicon-based aerogel thermal insulation materials: Performance optimization through composition and microstructure. J Non-Crystalline Solids, 2021, 553: 120517
3 Linhares T, Pessoa de Amorim MT, Durães L. Silica aerogel composites with embedded fibres: A review on their preparation, properties and applications. J Mater Chem A, 2019, 7: 22768–22802
4 Gurav JL, Jung IK, Park HH, *et al.* Silica aerogel: Synthesis and applications. J NanoMaterials, 2010, 2010: 1–11
5 Smirnova I, Gurikov P. Aerogel production: Current status, research directions, and future opportunities. J SuperCrit Fluids, 2018, 134: 228–233
6 Pisal AA, Venkateswara Rao A. Development of hydrophobic and optically transparent monolithic silica aerogels for window panel applications. J Porous Mater, 2016, 24: 685–695
7 Mazrouei-Sebdani Z, Begum H, Schoenwald S, *et al.* A review on silica aerogel-based materials for acoustic applications. J Non-Crystalline Solids, 2021, 562: 120770
8 Liu H, Xu Y, Tang C, *et al.* SiO_2 aerogel-embedded carbon foam composite with co-enhanced thermal insulation and mechanical properties. Ceramics Int, 2019, 45: 23393–23398
9 Jin X, Wu C, Wang H, *et al.* Synergistic reinforcement and multiscaled design of lightweight heat protection and insulation integrated composite with outstanding high-temperature resistance up to 2500°C. Compos Sci Tech, 2023, 232: 109878
10 Wang L, Feng J, Zhang S, *et al.* Dual-channel coextrusion printing strategy towards mechanically enhanced, flame retardant, and thermally stable polyimide-silica aerogels for thermal insulation. Additive Manufacturing, 2023, 71: 103583
11 Wilson SMW, Gabriel VA, Tezel FH. Adsorption of components from air on silica aerogels. Microporous Mesoporous Mater, 2020, 305: 110297
12 Berardi U, Sprengard C. An overview of and introduction to current researches on super insulating materials for high-performance buildings. Energy Buildings, 2020, 214: 109890
13 Yang F, Zhao X, Xue T, *et al.* Superhydrophobic polyvinylidene fluoride/polyimide nanofiber composite aerogels for thermal insulation under extremely humid and hot environment. Sci China Mater, 2020, 64: 1267–1277
14 Rashid AB, Shishir SI, Mahfuz MA, *et al.* Silica aerogel: Synthesis, characterization, applications, and recent advancements. Part Part Syst Charac, 2023, 40: 2200186
15 Feng J, Su BL, Xia H, *et al.* Printed aerogels: Chemistry, processing, and applications. Chem Soc Rev, 2021, 50: 3842–3888
16 Xu L, Zhu W, Chen Z, *et al.* Double-network MK resin-modified silica aerogels for high-temperature thermal insulation. ACS Appl Mater Interfaces, 2023, 15: 44238–44247
17 Liu F, He C, Jiang Y, *et al.* Carbon layer encapsulation strategy for designing multifunctional core-shell nanorod aerogels as high-temperature thermal superinsulators. Chem Eng J, 2023, 455: 140502
18 Li L, Yalcin B, Nguyen BN, *et al.* Flexible nanofiber-reinforced aerogel (xerogel) synthesis, manufacture, and characterization. ACS Appl Mater Interfaces, 2009, 1: 2491–2501
19 Kim CY, Lee JK, Kim BI. Synthesis and pore analysis of aerogel–glass fiber composites by ambient drying method. Colloids Surfs A-Physicochem Eng Aspects, 2008, 313-314: 179–182
20 Nadargi DY, Latthe SS, Hirashima H, *et al.* Studies on rheological

properties of methyltriethoxysilane (MTES) based flexible superhydrophobic silica aerogels. Microporous Mesoporous Mater, 2009, 117: 617–626
21 Yuan B, Ding S, Wang D, *et al.* Heat insulation properties of silica aerogel/glass fiber composites fabricated by press forming. Mater Lett, 2012, 75: 204–206
22 Kim GS, Hyun SH. Effect of mixing on thermal and mechanical properties of aerogel-PVB composites. J Mater Sci, 2003, 38: 1961–1966
23 Leventis N, Sadekar A, Chandrasekaran N, *et al.* Click synthesis of monolithic silicon carbide aerogels from polyacrylonitrile-coated 3D silica networks. Chem Mater, 2010, 22: 2790–2803
24 Meador MAB, Vivod SL, McCorkle L, *et al.* Reinforcing polymer cross-linked aerogels with carbon nanofibers. J Mater Chem, 2008, 18: 1843–1852
25 Cho J, Jang HG, Kim SY, *et al.* Flexible and coatable insulating silica aerogel/polyurethane composites *via* soft segment control. Compos Sci Tech, 2019, 171: 244–251
26 Kim HM, Noh YJ, Yu J, *et al.* Silica aerogel/polyvinyl alcohol (PVA) insulation composites with preserved aerogel pores using interfaces between the superhydrophobic aerogel and hydrophilic PVA solution. Compos Part A-Appl Sci Manuf, 2015, 75: 39–45
27 Lee H, Lee D, Cho J, *et al.* Super-insulating, flame-retardant, and flexible poly(dimethylsiloxane) composites based on silica aerogel. Compos Part A-Appl Sci Manuf, 2019, 123: 108–113
28 Lee KJ, Choe YJ, Kim YH, *et al.* Fabrication of silica aerogel composite blankets from an aqueous silica aerogel slurry. Ceramics Int, 2018, 44: 2204–2208
29 Wang L, Feng J, Jiang Y, *et al.* Ultraviolet-assisted direct-write printing strategy towards polyorganosiloxane-based aerogels with freeform geometry and outstanding thermal insulation performance. Chem Eng J, 2023, 455: 140818
30 Xia T, Yang H, Li J, *et al.* Interfacial modification and ultra-low concentration sol impregnation: A combined approach for tailoring the pore structure and improving the thermal insulation performance of fumed silica compact. Ceramics Int, 2019, 45: 2662–2666
31 Wang L, Feng J, Luo Y, *et al.* Three-dimensional-printed silica aerogels for thermal insulation by directly writing temperature-induced solidifiable inks. ACS Appl Mater Interfaces, 2021, 13: 40964–40975
32 Lu G, Wang XD, Duan YY, *et al.* Effects of non-ideal structures and high temperatures on the insulation properties of aerogel-based composite materials. J Non-Crystalline Solids, 2011, 357: 3822–3829
33 Jo HY, Oh SJ, Kim MN, *et al.* Effects of SiC particle size and inorganic binder on heat insulation of fumed silica-based heat insulation plates. J Korean Ceram Soc, 2016, 53: 386–392
34 Du H, Wang S, Xing Y, *et al.* The dual effect of zirconia fiber on the insulation and mechanical performance of the fumed silica-based thermal insulation material. Ceramics Int, 2022, 48: 6657–6662
35 Zhang S, Wang L, Feng J, *et al.* Fumed silica-derived, ambient dried, and low-cost nanoporous aerogel-like monoliths for thermal insulation. ACS Appl Nano Mater, 2023, 6: 10511–10520
36 Rubio J, Mazo MA, Martín-Ilana A, *et al.* FT-IR study of the hydrolysis and condensation of 3-(2-amino-ethylamino)propyl-trimethoxy silane. Boletín de la Sociedad Española de Cerámica y Vidrio, 2018, 57: 160–168
37 Yang HS, Choi SY, Hyun SH, *et al.* Ambient-dried low dielectric SiO_2 aerogel thin film. J Non-Crystalline Solids, 1997, 221: 151–156
38 Zu G, Shimizu T, Kanamori K, *et al.* Transparent, superflexible doubly cross-linked polyvinylpolymethylsiloxane aerogel superinsulators *via* ambient pressure drying. ACS Nano, 2018, 12: 521–532
39 Zu G, Kanamori K, Maeno A, *et al.* Superflexible multifunctional polyvinylpolydimethylsiloxane-based aerogels as efficient absorbents, thermal superinsulators, and strain sensors. Angew Chem Int Ed, 2018, 57: 9722–9727
40 Zu G, Kanamori K, Shimizu T, *et al.* Versatile double-cross-linking approach to transparent, machinable, supercompressible, highly bendable aerogel thermal superinsulators. Chem Mater, 2018, 30: 2759–2770
41 Li Z, Cheng X, He S, *et al.* Characteristics of ambient-pressure-dried aerogels synthesized *via* different surface modification methods. J Sol-Gel Sci Technol, 2015, 76: 138–149
42 Feng J, Wang Y, Feng X, *et al.* Radiative heat attenuation mechanisms for nanoporous thermal insulating composites. Appl Therm Eng, 2016, 105: 39–45

Acknowledgements This work was supported by Hunan Provincial Natural Science Foundation of China (2023JJ30632) and the Key R & D Program of Hunan Province (2022GK2027).

Author contributions Feng JZ and Feng J conceived the idea. Zhang S performed the experiments, analyzed the data and wrote the manuscript. Wang L performed partial experiments and tests. Jiang Y, Li L and Hu Y contributed to the theoretical analysis, supervision and editing. All authors contributed to the general discussion.

Conflict of interest The authors declare that they have no conflict of interest.

Supplementary information Supporting data are available in the online version of the paper.

Shunyao Zhang is currently a Master's candidate at the National University of Defense Technology. He obtained his BS degree (2021) in applied chemistry from Beijing Institute of Technology. His research mainly focuses on the design and preparation of low-cost silica aerogel composites and their thermal insulation applications.

Junzong Feng is an associate professor at the College of Aerospace Science and Engineering, the National University of Defense Technology (NUDT), China. He obtained his PhD degree in materials science and engineering from NUDT in 2012, and then joined the Aerogel Research group led by Professor Jian Feng. His research interests include the design, preparation, and characterization of nanoporous aerogels, specifically carbon and oxide aerogels, and their applications as superthermal insulators and catalyst supports.

基于水性气相二氧化硅浆料制备柔性二氧化硅气凝胶复合毡

张舜尧, 王鲁凯, 冯军宗*, 姜勇刚, 李良军, 胡艺洁, 冯坚

摘要 二氧化硅气凝胶由于其低导热率在隔热应用方面具有巨大的潜力. 然而, 它们通常具有较差的机械性能, 需要在保持低热导率的同时增强机械性能. 本研究以商业化气相二氧化硅和甲基三甲氧基硅烷为硅源, 并以水和乙醇为溶剂形成浆料. 基于此, 二氧化硅气凝胶块体(SAMs)可通过常压干燥进行制备, 且无需额外的表面改性或溶剂置换. 制备的SAMs保持了典型的纳米孔结构, 具有低密度(0.24 g cm^{-3})、收缩率(4%)和热导率(0.046 W m^{-1} K^{-1}). 通过辊压将浆料浸渍到纤维毡中, 并通过浆料热固化和常压干燥制备出二氧化硅气凝胶毡(SABs). 制备的SABs具有良好的柔韧性和机械性能, 便于安装和隔热应用, 并显著减少了生产周期和成本. 此外, 基于SAMs的纳米孔结构和低收缩率, 通过调控遮光剂的粒径和质量分数进一步降低了SABs的高温热导率, 优化后的SABs在800°C的热导率低至0.054 W m^{-1} K^{-1}.

